Received: 21 March 2022 | Revised: 14 September 2022 | Accepted: 20 September 2022

DOI: 10.1002/jbm.a.37450

RESEARCH ARTICLE

Society For Biomaterials WILEY

Optimization of methacrylated gelatin /layered double hydroxides nanocomposite cell-laden hydrogel bioinks with high printability for 3D extrusion bioprinting

Emine Alarçin[1] | Burçin İzbudak[2] | Elif Yüce Erarslan[3] | Sherif Domingo[3] | Rumeysa Tutar[4] | Kariman Titi[5] | Banu Kocaaga[6] | F. Seniha Guner[6] | Ayça Bal-Öztürk[2,7,8]

[1]Department of Pharmaceutical Technology, Faculty of Pharmacy, Marmara University, Istanbul, Turkey

[2]Department of Stem Cell and Tissue Engineering, Institute of Health Sciences, Istinye University, Istanbul, Turkey

[3]Chemical Engineering Department, Faculty of Engineering, Istanbul University-Cerrahpasa, Istanbul, Turkey

[4]Department of Chemistry, Faculty of Engineering, Istanbul University-Cerrahpasa, Istanbul, Turkey

[5]Department of Chemistry, Faculty of Science and Technology, Hebron University, Hebron, West Bank, Palestine

[6]Department of Chemical Engineering, Istanbul Technical University, Istanbul, Turkey

[7]Department of Analytical Chemistry, Faculty of Pharmacy, Istinye University, Istanbul, Turkey

[8]3D Bioprinting Design&Prototyping R&D Center, Istinye University, Istanbul, Turkey

Correspondence
Ayça Bal-Öztürk, Department of Stem Cell and Tissue Engineering, Institute of Health Sciences, Istinye University, 34010 Istanbul, Turkey.
Email: aycabal@gmail.com and aozturk@istinye.edu.tr

Funding information
Scientific and Technological Research Council of Turkey (TÜBİTAK), Grant/Award Number: 118S546

Abstract

Layered double hydroxides (LDHs) offer unique source of inspiration for design of bone mimetic biomaterials due to their superior mechanical properties, drug delivery capability and regulation cellular behaviors, particularly by divalent metal cations in their structure. Three-dimensional (3D) bioprinting of LDHs holds great promise as a novel strategy thanks to highly tunable physiochemical properties and shear-thinning ability of LDHs, which allow shape fidelity after deposition. Herein, we introduce a straightforward strategy for extrusion bioprinting of cell laden nanocomposite hydrogel bioink of gelatin methacryloyl (GelMA) biopolymer and LDHs nanoparticles. First, we synthesized LDHs by co-precipitation process and systematically examined the effect of LDHs addition on printing parameters such as printing pressure, extrusion rate, printing speed, and finally bioink printability in creating grid-like constructs. The developed hydrogel bioinks provided precise control over extrudability, extrusion uniformity, and structural integrity after deposition. Based on the printability and rheological analysis, the printability could be altered by controlling the concentration of LDHs, and printability was found to be ideal with the addition of 3 wt % LDHs. The addition of LDHs resulted in remarkably enhanced compressive strength from 652 kPa (G-LDH0) to 1168 kPa (G-LDH3). It was shown that the printed nanocomposite hydrogel scaffolds were able to support encapsulated osteoblast survival, spreading, and proliferation in the absence of any osteoinductive factors taking advantage of LDHs. In addition, cells encapsulated in G-LDH3 had a larger cell spreading area and higher cell aspect ratio than those encapsulated in G-LDH0. Altogether, the results demonstrated that the developed GelMA/LDHs nanocomposite hydrogel bioink revealed a high potential for extrusion bioprinting with high structural fidelity to fabricate implantable 3D hydrogel constructs for repair of bone defects.

KEYWORDS
3D bioprinting, hydrogel bioink, layered double hydroxide, nanocomposite scaffold

1 | INTRODUCTION

Bioprinting is an emerging strategy to generate 3D constructs based on layer-by-layer deposition of cell-laden biomaterials (bioink) with tailored architecture in accordance with computer-aided design.[1,2] This technique enables direct and precise control in the deposition of cell types, biomaterials and growth factors to recapitulate the structural and functional complexities of human tissue.[3,4] The main strategies for bioprinting include inkjet printing, extrusion printing, and laser-assisted printing.[5] Among them, extrusion bioprinting holds great promise attributed to its printing modality and utilization for various bioinks and curing strategy, an also relatively low cost.[6,7] Importantly, the bioprinting process and cellular response are strongly depends on the features of bioink. Hence, the selection of appropriate bioink combination for both successful printing and biological needs is still considered as one of major challenges in bioprinting process.[8,9] The bioink should be printable and quickly cross-linkable followed by printing.[1] The viscosity of the bioink should allow continuous extrusion, shape fidelity after extrusion, and avoid shear stress on cells during printing to overcome low cell viability.[10,11] In particular, shear-thinning materials provide an attractive solution to decrease shear stress inside nozzle during printing and then increase viscosity immediately after printing.[5] Furthermore, for a functional bioink development, it is crucial to have high biocompatibility, suitable biodegradability to provide new tissue formation and also structural and mechanical biomimetic properties to applied tissue.[10,12]

The use of hydrogel-based bioinks to encapsulate cells and/or bioactive compounds is a promising strategy due to recapitulating key properties of the natural extracellular matrix and providing highly aqueous 3D environment.[11,13,14] To date, various natural hydrogels consisting of collagen,[7,15] gelatin,[9,12] gelatin methacryloyl (GelMA),[6,16] silk fibroin,[17] and alginate[18,19] have been extensively explored as a bioink material in extrusion bioprinting. Among various hydrogel bioprinting materials, GelMA biopolymer has become most widely used material owing to its unique features such as outstanding biocompatibility and tunable characteristics and mechanical properties to better mimic native ECM.[20,21] Currently, Born and coworkers developed GelMA bioink for the release of extracellular vesicles and reduced initial burst release by increasing the concentration of cross linker during gelation.[22] Nevertheless, hydrogel based bioinks generally cannot meet all needs for direct bioprinting with high fidelity of constructs because of their limited printability,[6,23] insufficient rheological properties, slow gelation,[24] and inadequate mechanical strength.[25,26] In particular, it is demonstrated that GelMA bioinks could be printed at higher concentrations, but high concentrations exhibit a challenge for the survival of encapsulating cells.[24,27] These drawbacks could be overcome by blending GelMA with other hydrogels to form interpenetrating or semi-interpenetrating structure, and/or incorporation of inorganic materials.[28–30] GelMA/alginate bioinks have been comprehensively explored for their potential properties in extrusion bioprinting.[31–34] The printability of GelMA/alginate blends was found to be sufficient for total polymer concentration between 11% and 15%. However, higher polymer concentration resulted in lower number of live printed cells.[31] Wang and coworkers incorporated alginate sulfate (a sulfated glycosaminoglycan [sGAG] mimic) to GelMA/alginate blends for bioprinting of cartilaginous tissues where alginate sulfate improved bioprinting fidelity, and mesenchymal stem cell viability after printing.[34] In a recent study, GelMA/methacrylated silk fibroin bioinks were designed and the mechanical features of bioinks remarkably improved by the presence of methacrylated silk fibroin which is attributed to the increased polymeric chains content in the network and the high-crosslinking density.[35] In addition, synthetic polymers such as PLGA[36] and PCL[37] were blended GelMA to provide sufficient mechanical strength for bone tissue. Gaharwar and coworkers reported that kappa-carrageenan and nanosilicate particles in GelMA based bioinks could provide a great control of printability to obtain mechanically compatible cellularized constructs with high cellular activity.[28]

Recently, various nanocomposites hydrogels have been developed by using nanoparticles including graphene oxide, nanosilicate, reduced graphene oxide, and layered double hydroxides (LDHs) to enhance rheological and mechanical properties of material.[38–43] Compared to these nanoparticles, LDHs have represented a new field of interest due to their highly tunable features and controlled constitutes, and interlayer ion exchangeability as well as wide potential particularly in drug delivery, nanomedicine, and bioengineering.[44–47] LDHs are known as a class of anionic clay with positively charged Brucite ($Mg[OH]_2$) nanosheets less than 100 nm in diameter and exchangeable anions and water molecules located in the interlayer.[48–50] LDHs are typically demonstrated by the formula $[M^{2+}_{1-x}\ M^{3+}_{x}\ (OH)_2]\ [A^{n-}]_{x/n} \bullet zH_2O$, where M^{2+}, M^{3+}, and A are a divalent cations (Mg^{2+}, Fe^{2+}, or Co^{2+}), a trivalent cations (Al^{3+}, Fe^{3+}, or Gd^{3+}) and the interlayer exchangeable anions (Cl^-, CO_3^{2-}, NO_3^-), respectively.[47,51] As distinct from other clays, LDHs cannot swell spontaneously in water and their high surface charge and strong interaction between adjacent sheets make their delamination difficult.[43,44] Recently, LDHs have been used as additive to polymer matrix, drug delivery agent, osteogenic differentiation and antibacterial agent. In particular, LDHs sheets could disperse homogeneously within polymer matrix providing strong interfacial interaction in polymer network and eventually lead to enhancement in physico-mechanical properties.[46,52,53] Moreover, LDHs could form a mechanically stable network with shear-thinning characteristics.[46,53] For instance, Chakraborty and coworkers demonstrated that LDHs addition into poly (methyl methacrylate) (PMMA) network resulted in more thicker solution and significantly enhanced shear thinning behavior.[53] Importantly, the addition of LDHs remarkably improved osteogenic differentiation owing to their ionic content through generation of Mg^{2+} as well as alkaline micro-environment.[54] The presence of Mg^{2+} ions could allow an up regulation of the integrin expression of osteogenic cells.[55] Furthermore, Mg^{2+} ions could promote ALP activity of stem cells and osteogenesis signaling pathways.[56] In recent, various research groups have investigated the addition of LDHs into polymeric matrix for bone healing.[48,57–59] For instance, Fayyazbakhsh and coworkers reported that the mechanical properties, chemical composition and microstructure of LDHs/hydroxyapatite/gelatin constructs similar to native bone structure. The bone regeneration was accelerated followed implantation of these constructs to rabbit critical defect on the left radius bone.

Here, we describe a straightforward strategy for direct extrusion bioprinting of cell-laden hydrogel based scaffolds with high shape fidelity and

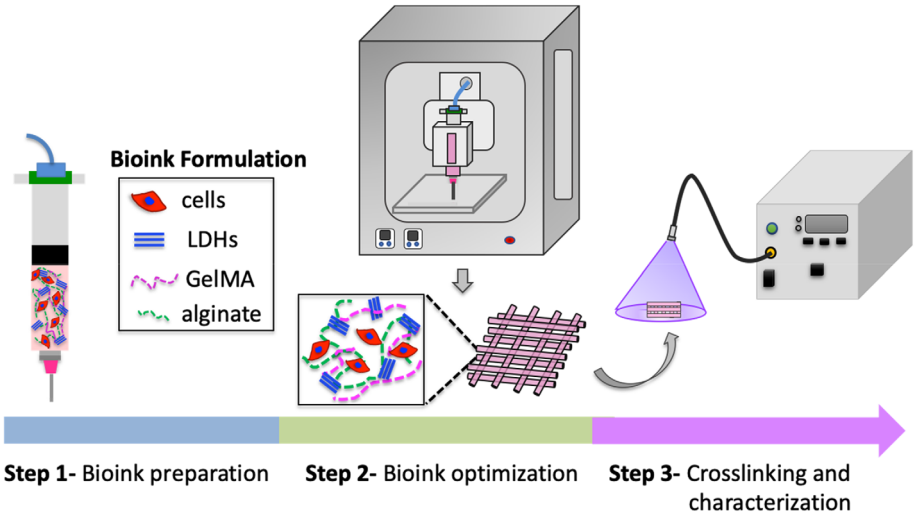

FIGURE 1 Schematic demonstrating the fabrication procedures of cell laden GelMA/LDHs hydrogel based nanocomposite scaffolds by using 3D extrusion bioprinting

improved bioactivity by combining GelMA, LDHs, and alginate for bone regeneration (Figure 1). To our knowledge, this is the first study to report the 3D bioprinting of cell-laden LDHs. In particular, the addition of LDHs could promote flow properties of GelMA hydrogel due to its self-healing and shear-thinning property, which allows significantly improved printability of structure. Moreover, LDHs could present osteogenic properties in the absence of osteoinductive factors. On the other hand, alginate was incorporated to the bioink composition in a small proportion to improve viscosity of GelMA through electrostatic interaction.[60] We first synthesized LDHs through co-precipitation method, and prepared various formulations to investigate their printability performance. Then, rheological properties, the mechanical and degradation characteristics of selected bioinks were investigated. Afterwards, osteoblasts were seeded onto the optimized bioinks to explore cellular adhesion. Finally, we encapsulated osteoblasts into nanocomposite bioinks and followed by printing of structure. These cell-laden hydrogel constructs were examined for cellular viability, cellular proliferation and spreading. We envision that the generation of GelMA/LDHs nanocomposite hydrogel bioink could present an applicable approach for bioprinting of scaffolds for bone regeneration.

2 | MATERIALS AND METHODS

2.1 | Materials

Magnesium nitrate hexahydrate ($Mg[NO_3]_2 \bullet 6H_2O$), sodium carbonate (Na_2CO_3), gelatin from porcine skin (type-A, 300 bloom), methacrylic anhydride (MA), aluminum nitrate nanohydrate ($Al[NO_3]_3 \bullet 9H_2O$), 2-hydroxy-1-[4-(2-hydroxyethoxy) phenyl]-2-methyl-1- propanone (Irgacure 2959), sodium alginate, 3-(4,5-dimethylthiazol-2-yl)-2,5-diphenyltetrazolium bromide (MTT), 4′,6-Diamidino-2-Phenylindole (DAPI) and dimethyl sulfoxide (DMSO) were purchased from Sigma-Aldrich (St. Louis, MO, USA). Low glucose- Dulbecco's Modified Eagle Media (L-DMEM), Fetal Bovine Serum (FBS), and Penicillin–Streptomycin (P/S) were obtained from GIBCO. Rhodamine-Phalloidin (AlexaFluor 594) dye, Live/Dead stain kit and PrestoBlue dye were obtained from Invitrogen.

2.2 | Synthesis and characterization of LDHs nanoparticles

2.2.1 | Synthesis of LDHs nanoparticles

LDHs were synthesized with previously described co-precipitation method with an Al/(Mg + Al) molar ratio of 0.25 in an alkaline environment at room temperature in nitrogen gas atmosphere.[61] Briefly, 93.75 mmol of $Mg(NO_3)_2 \bullet 6H_2O$ and 31.25 mmol of $Al(NO_3)_3 \bullet 9H_2O$ were dissolved in 250 ml of distilled water. This solution was added dropwise into an aqueous solution of 10 g NaOH and 3.312 g Na_2CO_3 in 250 ml of distilled water under constant agitation and then allowed to stir for 1 h. Subsequently, this suspension was filtered and washed with deionized water to provide neutralization. LDHs nanoparticles prepared using hydrothermal method.[62,63] Therefore, the obtained product was suspended in distilled water, incubated hydrothermally in an autoclave at 100°C for 16 h and dried by lyophilization for 48 h.

2.2.2 | Characterization of LDHs nanoparticles

To ensure the synthesis of LDHs, FTIR spectrum of LDHs was obtained at wavenumbers of 400–4000 cm^{-1} by using a FTIR spectrophotometry equipped with ATR sampling accessory (Jasco FT/IR-4600). X-ray diffraction (XRD) patterns of LDHs nanoparticles were obtained with CuKα radiation (λ-1.5418 Å) at 45 mA, 40 kV and Ni-filter (PANanalytical X'Pert Pro MPD Model XRD device). The chemical composition of the prepared LDHs nanoparticles was analyzed by using an Agilent 7800 Quadrupole inductively coupled plasma-mass spectrometer (ICP-MS). The Mg^{2+}/Al^{3+} ratio of LDHs nanoparticles was calculated based on concentrations determined by ICP-OES.

The surface morphology of synthesis LDHs nanoparticles was investigated using transmission electron microscopy (TEM-JEOL 1220 JEM) with 120 kV acceleration voltage at room temperature. The mean particle diameter, polydispersity index and zeta potential of LDHs nanoparticles were evaluated by using dynamic laser light scattering (Malvern Zetasizer Nano ZS, UK). Briefly, LDHs were diluted

appropriately with distilled water. Then, samples were analyzed in a capillary zeta cuvette (DTS1070 cuvette, Malvern Panalytical, Malvern, UK) at room temperature with a scattering angle of 90°. The stability of LDHs in distilled water was evaluated after 1 or 3 months storage at 4°C (refrigerator), 25°C and 60% relative humidity (RH), and 37°C and 75% RH. The zeta potential and particle size were investigated as described above to define stability.

2.3 | Synthesis and characterization of GelMA

2.3.1 | Synthesis of GelMA

GelMA was synthesized according to previous protocol.[64] Briefly, 10% (w/v) type A porcine skin gelatin was dissolved in Dulbecco's phosphate buffered saline (DPBS) by stirring at 50°C. Then, 5 ml of MA was added dropwise and allowed to stir for 2 h at 50°C. The reaction was stopped by fivefold dilution with DPBS at 50°C. Subsequently, the obtained GelMA solution was dialyzed against deionize water using a 12–14 kDa cutoff dialysis membrane for 7 days and GelMA solution was stored at −80°C, and then lyophilized.

2.3.2 | Characterization of GelMA

FTIR spectrums of gelatin and GelMA were collected as described above to determine the formation of GelMA. To obtain ^{1}H NMR spectrum, gelatin and synthesized GelMA was dissolved in deuterium oxide at 40°C. ^{1}H NMR spectrum was obtained at 40°C and a resonance frequency of 500 MHz by Varian UNITY INOVA NMR spectrometer. Methacrylation degree was calculated based on ^{1}H NMR spectra of GelMA as the ratio between the numbers of methacrylated groups attached to the gelatin and the total number of amine units on the unmodified gelatin prior to reaction. To define the methacrylation degree, we normalized the spectra based on the phenylalanine signal (7.0–7.5 ppm) which is related to gelatin concentrations.[65]

2.4 | 3D bioprinting of GelMA/LDHs nanocomposite bioinks

2.4.1 | Preparation of GelMA/LDHs nanocomposite bioinks

Synthesized LDHs nanoparticles were dispersed in PBS solution including 0.25% (w/v) photoinitiator (Irgacure 2959) at 50°C for 2 h. GelMA (15% [w/v]) was fully dissolved in obtained dispersions containing 0%, 1%, 3%, 5%, 7%, and 10% (w/v)LDHs nanoparticles. Thereafter, 1% (w/v) alginate was added and stirred at 50°C for 1 h. Final bioink solution was obtained by mixing overnight at room temperature and before bioprinting, transferred into a 5 ml syringe (EFD Syringe Barrel).

2.4.2 | Bioprinting

A commercial bioprinter (Axodual Bioprinter, Axolotl Biosystems) with computer-assisted software was used to print the constructs. All the bioprinting studies were performed by using 25G nozzle with pressure value of 35–40 psi. Immediately after printing, bioprinted constructs were photo cross-linked using UV light (360–480 nm) for 40 s at 6.9 W cm^{-2} (OmniCure S2000, Excelitas Technologies, USA) to maintain printed constructs.

2.4.3 | Bioink optimization

Printability

Developed bioink was placed into a 5 ml syringe and 25G blunt needle fixed to this syringe using a luer lock mechanism. The minimum pneumatic pressure to extrude the bioink through steady fiber flow was determined as extrusion pressure. The printability of bioink with various concentrations of LDHs nanoparticles (0, 1, 3, 5, 7, and 10 wt % of GelMA amount in bioink composition), GelMA (15% [w/v]) and alginate (1% [w/v]) were evaluated according to generating continuous, complete and reproducible constucts, after bioprinting. Herein, printing pressure (0–50 Psi) and printing speed (1–50 mms^{-1}) were optimized. The bioink printability value (Pr) was determined using Image-J software to evaluate the area and perimeter of interconnected pores.[66,67] Pr is calculated using following equation:

$$\mathrm{Pr} = \frac{L^2}{16A} \quad (1)$$

where L is perimeter and A is area.

Rheological measurements

The rheological properties of blend bioinks with various LDHs concentrations were determined by a rotational rheometer (Anton Paar MCR 301) with a 25 mm diameter, parallel plate geometry, and 0.9–1 mm plate-to-plate distance at room temperature. Strain sweep test at an angular frequency of 10 rad s^{-1} was carried out to detect the linear viscoelastic region in the oscillation mode. Then, the frequency sweep test was performed in the range of 0.1 to 100 rad s^{-1} at 1% shear strain to establish the storage (G′) and loss modulus (G″) of the samples.

2.5 | Characterization of 3D bioprinted constructs

2.5.1 | FTIR and SEM analysis

To demonstrate the structure of nanocomposite scaffolds, FTIR-ATR spectroscopy scanning was performed as described above. The morphology of the 3D printed nanocomposite scaffolds was investigated by field emission scanning electron microscopy attached with an energy-dispersive X-ray spectroscopy (FEGSEM-EDS; FEI ESEM Quanta 450 FEG). Before imaging, the lyophilized constructs were

sputter-coated with a thin layer of gold. Thereafter, the porosity of printed constructs was calculated by using SEM images along with Image-J software ($n = 4$).

2.5.2 | Mechanical properties

The mechanical features of composite bioinks were measured after UV crosslinking by compression tests using a mechanical testing machine (TA Instruments). Briefly, composite bioinks with various concentrations of LDHs nanoparticles were prepared by molding technique by pipetting 100 µl of bioink mixture, followed by exposing to 6.9 W cm^{-2} for 40 s. Thereafter, cylindrical samples with diameter of 5 mm were obtained using a biopsy punch. The obtained constructs were placed on the platen and compressive strength were measured at a cross speed of 1 mm s^{-1} and a 60% strain level. The compressive modulus was reported as the slope of the linear region in the 0%–10% strain ($n = 4$).

2.5.3 | Swelling

To determine the swelling rate of nanocomposite scaffolds, constructs were soaked in 3.0 ml of PBS at 37°C for 24 h ($n = 4$). Then, the swollen constructs were removed from PBS, and the weights of samples were recorded after removal of excess water from surface of constructs using a filter paper. The swelling rate was calculated based on the ratio between the weight gain and the initial weight.

2.5.4 | Degradation

The degradation behavior of nanocomposite scaffolds was assessed in PBS at physiological temperature 37°C for up to 28 days ($n = 4$). After defined time points, the samples were carefully rinsed in distilled water, lyophilized, and then weight was recorded. The degradation rate was reported as the ratio between the weight remaining and the initial weight of construct.

2.6 | Cell culture

MC3T3-E1 cells (ATCC® CRL-2593) were cultured in L-DMEM containing 10% FBS ve 1% P/S. MC3T3-E1 cells were incubated at 37°C in 5% CO_2 in a 75 cm^2 culture dish, and culture media was replaced every 2 days. Cells were passaged when they reached 80%–90% confluency and passage 6 was used in the further experiments.

2.6.1 | Biocompatibility of LDHs nanoparticles

To determine the biocompatibility of synthetized LDHs, MTT assay was performed. In brief, the cells were seeded into 48-well culture dishes at cell density of 1×10^4 cells/well, and culture dishes were incubated for 24 h at 37°C in 5% CO_2 to allow cell adhesion and spreading. After discarding cell culture medium, cell culture medium containing different concentrations of sterile LDHs nanoparticles (0.5, 1, 2, 3, 5, 7, 10 ve 15 mg/ml) were added, and incubated at 37°C in 5% CO_2 for 48 h. Untreated cells incubated in the culture media was considered as the positive control, while the cells incubated in DMSO was considered as negative control.[68] Subsequently, the cell culture medium containing nanoparticles was removed, MTT solution (0.5 mg/ml) was added to each well and incubated at 37°C for 4 h. After incubation, the solution was removed, DMSO was added and incubated for another 10 min. The optical density of plates was measured using a microplate reader (SpektrostarNano) at 570 nm. The cell culture medium was considered as 100% and the other samples were calculated accordingly ($n = 6$).

2.6.2 | In vitro cell adhesion studies

To evaluate cell adhesion and spreading as a function of concentration of LDHs, osteoblast cells (4×10^4 cells/well) were seeded on nanocomposite scaffolds. The morphology of cells seeded on nanocomposite constructs was determined by Rhodamine-Phalloidin and DAPI staining according to the manufacturer's instructions. Briefly, the samples were rinsed in PBS, fixed with 4% (w/v) paraformaldehyde for 20 min, and washed with PBS. Subsequently, the samples were treated with 0.05% (v/v) Triton X-100 for 20 min to permeabilize the cell membrane, and blocked with 5% (w/v) rabbit serum albumin for 1 h. For F-actin cytoskeleton staining, the samples were incubated with Rhodamine-Phalloidin for 1 h at 37°C. Finally, the nuclei was stained by incubation with DAPI for 30 min at 37°C, and the samples were visualized by fluorescence microscopy (Zeiss AxioScope Z1). Rhodamine-Phalloidin and DAPI staining were performed at days 1, 3, and 7 after cell seeding on construct including 0, 1, 3, 5, and 10 wt % LDHs ($n = 4$).

2.6.3 | Bioprinting of cell-encapsulated nanocomposite scaffolds

For cell encapsulation, the cells were trypsinized, counted, 3×10^6 cells ml^{-1} of osteoblasts gently mixed with GelMA/LDHs nanocomposite bioinks at 37°C and then transferred into syringe for bioprinting. Subsequently, cell encapsulated bioinks were printed and exposed to UV light at a power of 3.95 mW/cm^2 for 40 s. Cell encapsulated nanocomposite scaffolds were cultured for a certain time period (1, 3, 7 days) at 37°C with 5% CO_2. The culture media was changed every 2 days.

2.6.4 | Cell viability, proliferation and spreading assay

Cell viability was evaluated by Live/Dead test according to the manufacturer's instructions. In brief, the samples were incubated with

calcein-AM (green) and ethidium homodimer-1 (red) for 20 min, and washed with PBS. Finally, stained samples were observed under inverted fluorescence microscope. For each hydrogel formulation, at least six different areas of the three-bioprinted scaffolds were analyzed using Image-J software. The cell viability was reported as the percentage of the number of live cells to total cells. The cell viability was evaluated at days 1, 3, and 7 after bioprinting of cell laden G-LDH0 and G-LDH3 ($n = 3$).

The metabolic activity of cells was determined by PrestoBlue assay according to the manufacturer's instructions. Briefly, the culture media was changed with DMEM containing 10% (w/v) PrestoBlue, and incubated for 1 h at 37°C. Then, supernatant was collected, and the fluorescence of the reduced PrestoBlue dye was measured at 570 (excitation) and 600 nm (emission). The bioprinted constructs without cell encapsulation were used as control, and the OD values were normalized to the initial OD value of day 0. The metabolic activity was evaluated at days 0, 1, 3, and 7 after bioprinting ($n = 6$).

The nuclei and actin fibers of cells were stained with DAPI and rhodamine-phalloidin to observe the morphology and spreading of osteoblast cells in bioprinted constructs according to previously described method ($n = 3$). To quantify the morphological differences, mean cell area, and cell aspect ratio (long/short axis) were calculated according to the literature.[69–71]

2.7 | Statistical analysis

All experiments were performed at least three times, and all results were given as mean ± standard deviation (SD). Statistical analysis in this study were carried out using One-way ANOVA with ±95% confidence interval (ns > 0.05,*p < 0.05, **p < 0.01; ***p < 0.001).

3 | RESULTS AND DISCUSSION

3.1 | Synthesis and characterization of LDHs nanoparticles

LDHs, 2D hydrotalcite compounds (Figure 2A), have great potential for tissue engineering and drug delivery applications.[62,72,73] Herein, cell-laden LDHs/GelMA/alginate nanocomposite bioinks were developed for extrusion bioprinting. Firstly, LDHs were synthesized by a straightforward and generally applicable hydrothermal method. It was demonstrated that LDHs nanoparticles were synthesized successfully through FTIR, XRD and ICP-OES analysis.

Figure 2B displays the FTIR spectrum of LDHs where the absorption band between 558 and 657 cm^{-1} attributed to the octahedral compound of MgO_6 and AlO_6. The sharp absorption peak at 1365 cm^{-1} showed the presence of sufficient nitrate ions in the intermediate layer. The wide absorption band corresponding to the stretching vibrations of —OH units of interlayer water and structural hydroxyl units in the LDHs was observed between 2700 and 3900 cm^{-1}. A shoulder at 1640 cm^{-1} ascribed to the bending deformation of water.[74,75]

XRD pattern of LDHs was further evaluated to define the crystalline structure (Figure 2C). The XRD pattern demonstrated the presence of three intense reflection peaks at 2θ angles at 11.38, 22.93, 34.52° indicating the interlayer intervals of LDHs in the d_{003} plane (7.775 Å), in the d_{006} plane (3.878 Å) and in the d_{009} plane (2.598 Å), respectively. The obtained XRD pattern confirmed that LDHs nanoparticles had a layered and crystalline structure and were agreement in previous works.[76,77]

To determine the Mg and Al content, ICP-MS analysis was performed. Based on ICP-MS analysis, Mg and Al amount in LDHs was found as 22.64 (%w) and 9.51 (%w), respectively, and the calculated mole ratio of Mg^{2+}/ Al^{3+} cations (2.64) were close to expected theoretical value.[78]

The size of synthesized LDHs was found to be 78.33 ± 31.15 nm and the PDI value of 0.210 (Figure 2D). The zeta potential of LDHs was measured as +25.6 ± 6.19 mV indicating physical stability of nanoparticles.[79] Based on TEM analysis, the particle size of LDHs was around 55–105 nm in a consistency with DLS results (Figure 2E).

The biocompatibility of LDHs was evaluated by using MTT assay, a widely used colorimetric method based on enzyme activity to determine the number of living cells. After 48 h of incubation, LDHs in the concentration of 0.5–15 mg/ml were found to be non-toxic on osteoblast cells (Figure 2F). Previously, Wu et al. demonstrated that Mg/Al (molar ratio 3: 1) LDHs nanoparticles (2–40 μg/ml) exhibited no toxic effects on embryonic stem cells (mESC) by MTT analysis.[80] Similarly, LDHs showed no toxic effect on preosteoblast cells up to a concentration of 0.02 mg / ml.[81] Overall, it is concluded that LDHs are biocompatible and safe to be used in tissue engineering applications.

To investigate the stability of suspensions of LDHs in distilled water, the particle size and zeta potential were determined after storage of these suspensions at 4°C (refrigerator), 25°C and 60% RH, and 37°C and 75% RH for certain periods (Table S1, Figure S1). Particle size of LDHs in suspensions was gradually increased for all conditions, as we expected. Based on stability tests, it can be concluded that the stability of the LDHs in suspension remained stable under all conditions for 1 week, while they were unstable at the end of the first month; determined by an increase in particle size. Important to note that the most favorable results were obtained from LDHs suspensions stored in 37°C and 75% RH where the particle sizes increased to 487.5 nm and the zeta potentials decreased to +18.8 mV from +25.6 mV.

3.2 | Synthesis and characterization of GelMA

In the present study, GelMA was successfully synthesized using previously described method, and the chemical composition of GelMA was determined by FTIR and ^1H NMR spectra. Figure S2A displays the FTIR spectra of gelatin and GelMA. The characteristic peaks at 1625 cm^{-1} (amide I), 1522 cm^{-1} (amide II), and 1440 cm^{-1} (amide III) were attributed to the stress vibration of the —C═O bond, the

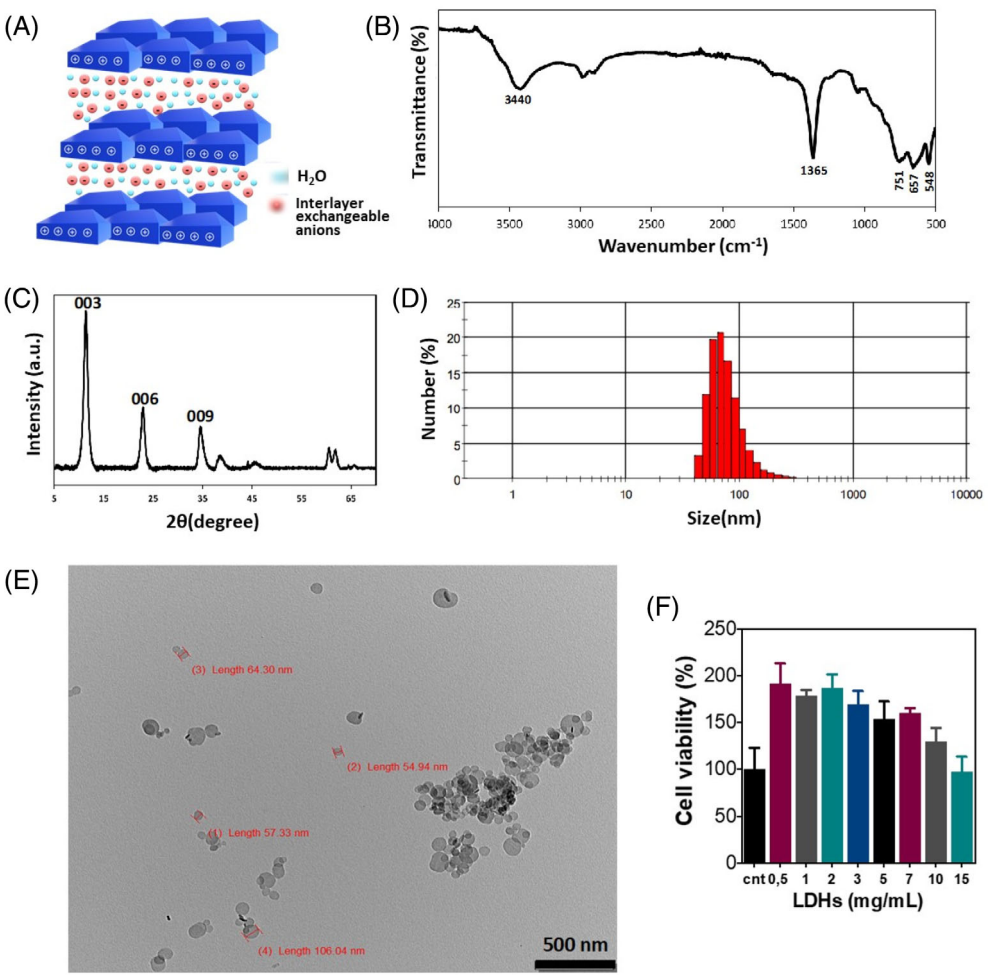

FIGURE 2 Characterization of synthetized LDHs (A) Schematic representation of the structure of LDHs, (B) FTIR spectra of LDHs, (C) XRD pattern showing the layered and crystalline structure of LDHs, (D) The DLS measurements demonstrated the size of LDHs with an average diameter of 78.33 nm and the PDI value of 0.210, (E) TEM image of LDHs (30,000× magnification) indicating particle size around 55–105 nm, and (F) MTT assay indicates that LDHs (0.5–15 mg/ml) were non-toxic on osteoblast cells after 48 h of incubation ($n = 6$). The bar graph demonstrates the average ± standard deviation (SD) bars.

bending vibration of the NH bond and in-plane bending vibration of the CN and NH bonds, respectively.[82] It is important to note that the intensity of amide peaks increased after methacrylation. Additionally, the peaks at 3260 and 2915 cm^{-1} were ascribed to O—H and C—H stress vibrations, respectively.[83] The FTIR data confirmed the methacrylation of gelatin.

In the ^{1}H NMR spectra of GelMA (Figure S2B), the peaks determined at 5.4 and 5.7 ppm indicating alkenyl double bond of methacrylate units linked to gelatin.[83] These results were confirmed the successful synthesis of GelMA polymer in agreement with the FTIR data.

3.3 | Printability assessment

3.3.1 | Printability

A commercial extrusion bioprinter was utilized to generate highly organized printed structures. G-code was written to define the movement of the robotic stage in X-Y-Z directions and also the actuation of the pneumatic valves. The generation of complex 3D architectures in bioprinting requires controlled deposition of bioink in sequential layers with well-defined geometry, and integrity.[10] Therefore, first we systematically optimized the bioink formulation to determine the optimal composition of bioink to obtain continuous filament formation for extrusion uniformity and then achieve 3D structures with high shape fidelity. Bioprinting process was conducted at 25°C, using a 25G needle. Firstly, we tried to print GelMA (15% w/v) alone. However, the obtained structure could not maintain the defined geometry due to low viscosity of GelMA resulted in the fluxion of the material. Subsequently, alginate was incorporated to GelMA to enhance viscosity of bioink and the shape fidelity. This increase in viscosity could be considered a result of electrostatic interactions between negatively charged alginate and positively charged GelMA (type-A gelatin).[60] The addition of alginate allowed printing of the 5-layered grid structure, using a 25G needle. Based on these initial experiments, bioink formulation consisted of 15% (w/v) GelMA and 1% (w/v) alginate was found to be sufficient for printing to maintain 3D architecture.

The printability and mechanical properties of bioink could be tuned by varying LDHs amount, resulting in accelerated cell proliferation. Therefore, we printed GelMA (15% w/v), alginate (1% w/v) and different amount of LDHs (0, 1, 3, 5, 7, and 10 wt % of GelMA amount in bioink composition) at 5-, 10-, 15- and 20- layered grid structure (Figure 3A, Figure S3). The bioink formulation without LDHs nanoparticles could be printed at only 5-layered structures. Notably, the printability of bioinks was improved with increasing concentration of

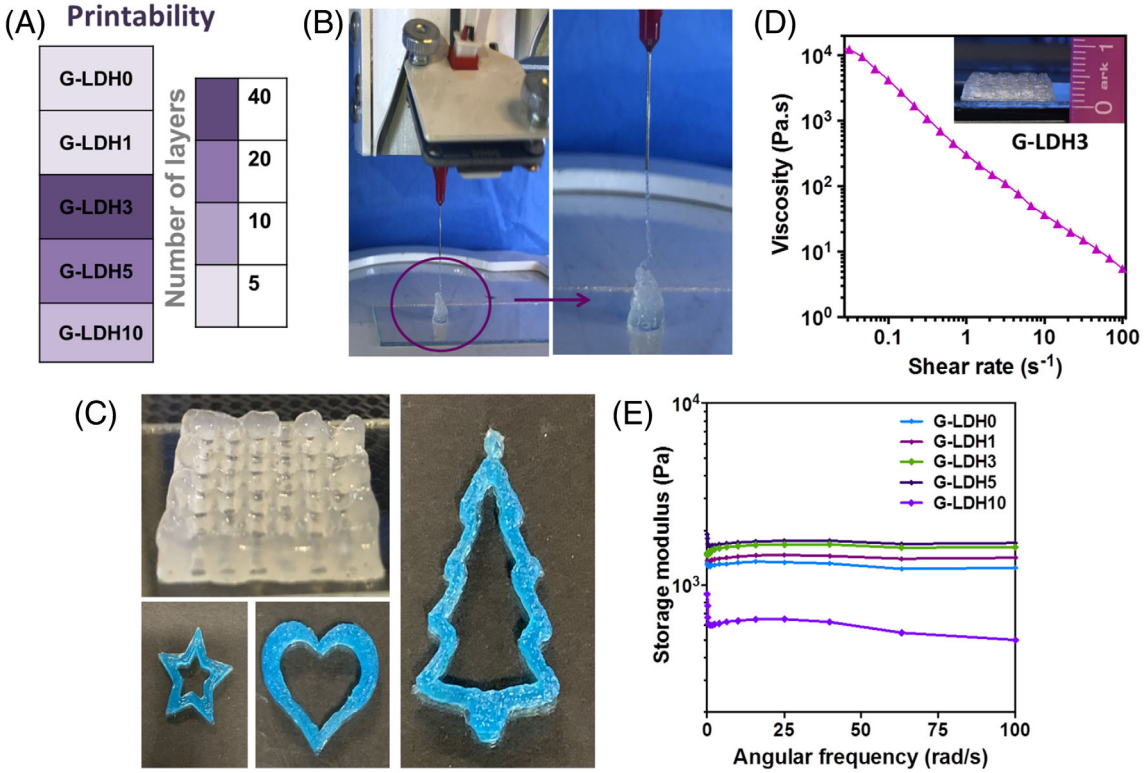

FIGURE 3 Printability and rheological studies to determine adequate concentration of LDHs, (A) Printability of various bioinks based on final printed layers without deformation, (B) Air extrusion of G-LDH3 showing filament formation and extrusion uniformity, (C) Photographs demonstrating various bioprinted structures (G-LDH3 bioink) with lack of noticeable deformation, including 20-layered grid structure, star, heart, and pine tree shaped structure, (D) Viscosity shear rate of G-LDH3. Viscosity of G-LDH-3 as a function of shear rate demonstrates shear-thinning characteristic of nanocomposite bioink formulation, and (E) Analysis of storage modulus by frequency sweep of GelMA/LDHs nanocomposite bioinks performed at 1% shear strain at various LDHs concentration ($n = 3$)

LDHs. The best printability and continuous filament formation were achieved with the formulation containing 3 wt % LDHs at 20-layered grid structures (Figure 3B,C). However, LDHs concentrations above 3 wt % in the formulation resulted in aggregation of nanoparticles as well as a highly viscous bioink and were printed by higher pressures. However, they still presented better printability and 3D shape fidelity after printing compared to LDHs free bioink compositions. For instance, bioink composition including 10 wt % LDHs enabled to print 10-layered structures in a well-defined geometry, while the LDHs free bioink composition enabled to print only 5-layered structures. Additionally, the structural fidelity was determined by printing of various 3D constructs such as star, heart, and pine tree shaped architectures (Figure 3C).

Importantly, for an a perfect gelation condition or favorable printability, the interconnected channels of the constructs could show square shape. Accordingly, the ideal gelation occurs when the Pr value is equal to 1, and thus smooth structures could be created.[66,67,84] It is also stated that the higher Pr value leads to greater gelation degree of the bioink and non-uniform printed morphology. Herein, Pr values for G-LDH0 and G-LDH3 were calculated using Equation (1), and found to be 1.14 ± 0.091 and 1.04 ± 0.076, respectively. It was demonstrated that the Pr value of G-LDH3 is closer to 1 with a better morphology compared to G-LDH0.

3.3.2 | Rheological evaluations

Rheology measurements were conducted to characterize shear rate-dependent viscosity and the storage modulus (G') and the loss modulus (G") of the materials. Even though the bioink composition with high viscosity is sufficient to maintain the printed structure, higher viscosity could decrease the cellular viability owing to applied shear forces during extrusion. The flow behavior could be explained by the relationship between viscosity and shear rate. The viscosity of bioinks incorporated with LDHs reduced with increasing shear rate, pointing out shear-thinning feature to allow favorable extrusion without clogging or cellular damage. The viscosity results of G-LDH3 bioink, have the best printability, was shown in Figure 3D. Afterwards, the frequency sweep was conducted below LVE region of material. G' and G" were determined against frequency (Figure 3E). G' and G" could be associated with extrudability and post printing shape fidelity. Herein, G' is an indicator of elastic behavior of bioink while G" is an indicator of the viscous fraction or dissipated energy of bioink composition. For sufficient printing process, the bioink should represent an elastic nature to allow regular filaments with structural fidelity and also viscous nature to flow from needle during extrusion.[85] Except for the G-LDH0 sample, the frequency sweep of the bioinks showed that G′ values slightly improved with the increasing LDHs concentration,

under the same conditions. G-LDH0 exhibited minimal G′ as about 1305 Pa and for G-LDH1, G-LDH3, and G-LDH5, G′ is as about 1403, 1588, and 1699 Pa, respectively. Previously, Heilshorn and colleagues reported that gels (G' > G") allow increased cell viability for injectable cell therapies.[86] Here, the obtained results of frequency sweep indicated a stable ink with higher G′ values over G″ at all frequencies (Figure S4). For a more sensitive comparison of the samples, the damping factor (tan δ) which is the ratio of G" to G' for the shear rate range of 0.1 to 100 rad s^{-1} was calculated for each sample (Figure S4G). Relatively low tan δ implies a higher stiffness and better printability. As shown in Figure S4G, G-LDH3 is one of the samples having with a low tan δ value.

3.4 | Characterization of 3D bioprinted hydrogel constructs

3.4.1 | FTIR and SEM analysis

To demonstrate the UV cross-linked structure, the developed GelMA/LDHs hydrogel based nanocomposite scaffolds were analyzed by FTIR-ATR spectroscopy scanning in the range of 400–4000 cm^{-1}. The FTIR spectra of the GelMA polymer and the developed GelMA/LDHs hydrogel based nanocomposite scaffolds are given in Figure 4A. For all nanocomposite scaffolds and GelMA, typical amide I and II bands were presented at 1640 and 1540 cm^{-1} due to C═O stretching and N—H bending, respectively. In particular, for GelMA/LDHs hydrogel based nanocomposite scaffolds, the intensity of the band appeared at 3010 cm^{-1} of the C—C bond decreased, pointing out the success of photo polymerization in accordance with previous literature.[83,87]

As shown in Figure 4B, LDHs exhibit a homogeneous distribution in nanocomposite scaffolds without any particle accumulation or aggregation. The porosities and pore diameters of scaffolds were determined according to SEM pictures using ImageJ software (National Institutes of Health, Bethesda, MD, USA). It is known that dense structures could result in a higher elastic modulus, which can result in undesired effects in cellular behavior, making it difficult for spreading of biomolecules in the cell environment to hydrogel.[88] On the contrary, in the current study, G-LDH3 with higher mechanical strength revealed higher porosity. Particularly, all scaffolds showed high porosity, which is required to allow the growth of encapsulated cells and transportation of oxygen and nutrients. The porosity slightly increased from 77.47% to 80.1% for G-LDH0 and G-LDH3. Importantly, the pore size of G-LDH0 and G-LDH3 were significantly enhanced from 81.93 ± 16.35 μm to 106.75 ± 51.92 μm, respectively.

3.4.2 | Mechanical properties

The crosslink density of the polymer networks enables to improve the stiffness of the bioprinted nanocomposite scaffolds. The assembly of the inorganic nanoparticles such as LDHs also could improve the stiffness and mechanical performance of the structure. It is well known that the mechanical features of bioprinted hydrogel constructs have a vital role to provide cell proliferation, migration, and differentiation as well as maintain their structure during surgical implantation.[28]

To investigate mechanical behaviors of hydrogels, compression tests were performed. The effect of the amount of LDHs on the mechanical properties of hydrogels was also evaluated (Figure 4C). As seen in Figure 4D, the compressive strength was 652 ± 188 kPa for the pristine GelMA hydrogel (G-LDH0), while it was significantly increased to 955 ± 1113 kPa and 1168 ± 31 kPa for G-LDH1 and G-LDH3, respectively. However, further increases in the concentration of LDHs provide a gradual reduction in compression modulus. For instance, G-LDH5, and G-LDH10 revealed compression modules as 924 ± 120 kPa and 741 ± 197 kPa. It was also confirmed that elongation (%) values at break showed a slight increase with the addition of LDHs. Elongation (%) values at break of hydrogels coded with G-LDH0, G-LDH1, G-LDH3, G-LDH5 and G-LDH10 was found to be 76.78% ± 5.11%, 84.76% ± 2.41%, 85.17% ± 0.3%, 83.42% ± 3.04%, and 81.70% ± 1.42%, respectively.

The elastic modulus of the scaffolds was developed by calculating the slope of the linear region in the 0%–10% strain range of the stress–strain curves (Figure 4E). Elastic modulus showed a similar trend with compression strength of gels. Elastic modulus of GelMA hydrogel scaffolds were improved by the 1 and 3 wt % LDHs addition to the formulation from 78.79 ± 3.44 kPa to 88.09 ± 5.72 kPa and 109.14 ± 4.02 kPa respectively. Elastic modulus decreased by further increase in the amount of LDHs such as G-LDH5, and G-LDH10 (98.87 ± 7.76 kPa and 91.69 ± 5.20, respectively). Importantly, it was still significantly higher than LDHs free GelMA.

3.4.3 | Swelling and degradation study

Swelling properties of nanocomposite scaffolds were demonstrated in Figure 4F. The swelling capacity was high for all scaffolds due to their highly interconnected porous structures. In particular, it was altered as a function of the amount of LDHs. Swelling equilibrium was occurred in about 24 h. After 24 h of incubation, the swelling ratio was found to be 568.44% ± 21.45%, 526.47% ± 17.84%, 501.39% ± 18.42%, 518.22% ± 21.2% and 541.97% ± 18.31% for G-LDH0, G-LDH1, G-LDH3, G-LDH5, and G-LDH10, respectively.

The degradation rate is a key factor in bone regeneration that should be in a consistency with new bone formation. In particular, degradation was significantly governed by the amount of LDHs (Figure 4G). For instance, after 1 week incubation, degradation rates were 64.1% ± 6.8%, 79.25% ± 7.65%, 89.79% ± 8.72%, 91.57% ± 7.58%, and 71.29% ± 9.17% weight remaining for G-LDH0, G-LDH1, G-LDH3, G-LDH5, and G-LDH10, respectively. G-LDH0 was degraded completely after 4 weeks incubation, while G-LDH1, G-LDH3, G-LDH5, and G-LDH10 experienced

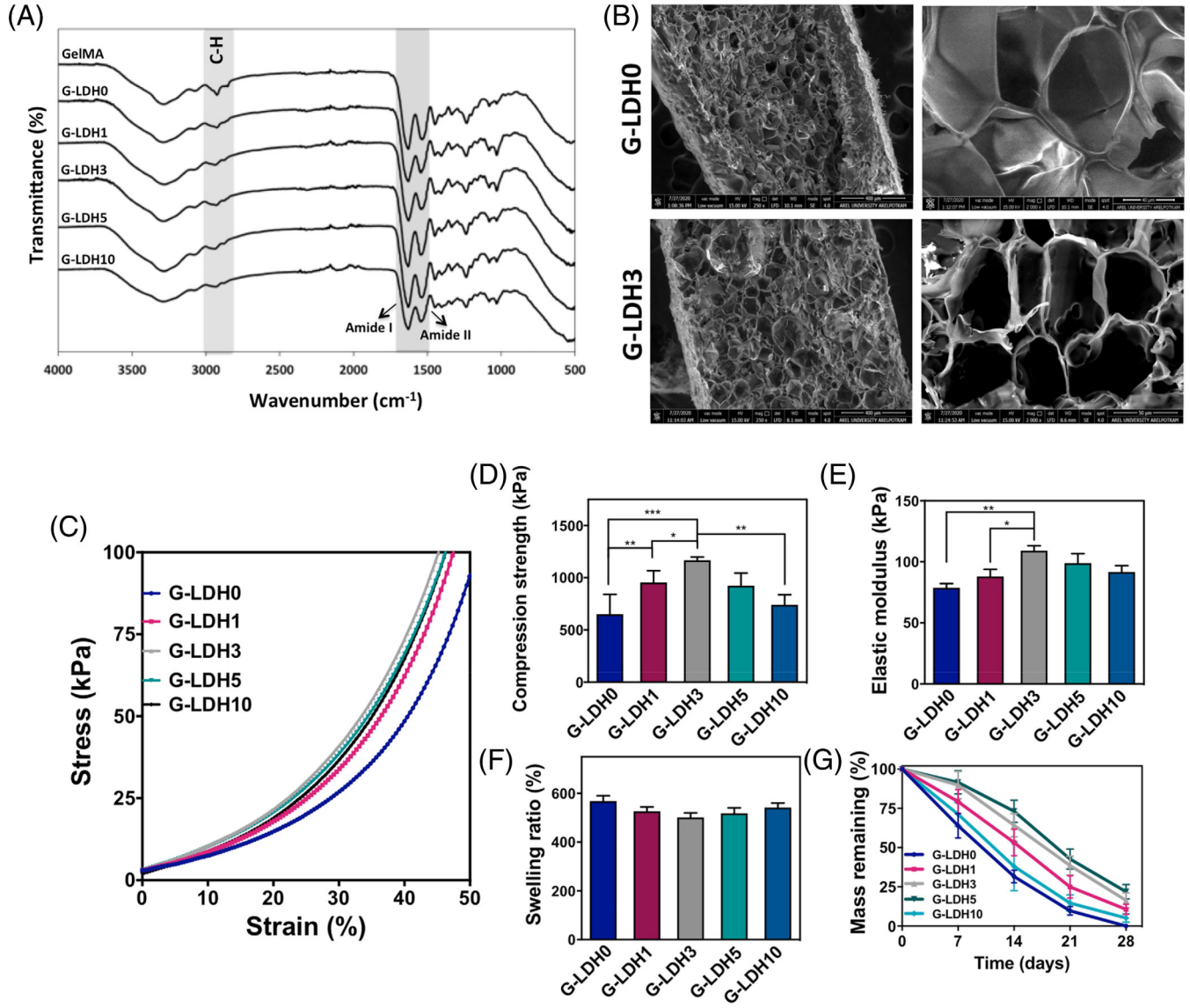

FIGURE 4 In vitro characterization of nanocomposite GelMA/LDHs hydrogel based nanocomposite constructs. (A) FTIR spectra of GelMA and GelMA/LDHs nanocomposite constructs, (B) Scanning electron microscopy (SEM) images with low (left side) and high (right side) magnifications of G-LDH0 and G-LDH3 show gradual changes in the microstructure of nanocomposite scaffolds, (C) Stress–strain curves of GelMA/LDHs nanocomposite scaffolds, (D) Compression strength of GelMA/LDHs nanocomposite scaffolds which showed a similar trend with elastic modulus, (E) The elastic modulus of the scaffolds was calculated from the slope of 0%–10% strain range. Elastic modulus of GelMA/LDHs nanocomposite scaffolds, which was enhanced with the presence of LDHs ($n = 4$), (F) Swelling ratio of GelMA/LDHs nanocomposite scaffolds which decreased by the addition of LDHs ($n = 4$), and (G) Degradation profile of GelMA/LDHs nanocomposite scaffolds. The presence of LDHs leaded to longer degradation time ($n = 4$). The graphs demonstrate the average ± standard deviation (SD) bars. (ns > 0.05,*p < .05, **p < .01; ***p < .001)

degradation with 10.7% ± 3.28%, 16.4% ± 4.79%, 21.89% ± 4.58%, and 5.16% ± 2.62% weight remaining in 4 weeks incubation. The addition LDHs to GelMA network remarkably enhanced the structural stability of the constructs resulted in longer degradation time. However, G-LDH10 exhibited a quite faster degradation rate compared to G-LDH5 due particle aggregation in high LDHs amount. Importantly, the degradation rate of G-LDH10 was still slower than G-LDH0.

3.5 | Cell culture

3.5.1 | In vitro cell adhesion studies

Since cellular adhesion is one of the crucial parameters for biomedical applications, we further evaluated the effect of GelMA and GelMA/LDHs hydrogel based nanocomposite scaffolds on cell adhesion behaviors of osteoblast cells. The fluorescence microscopic images of

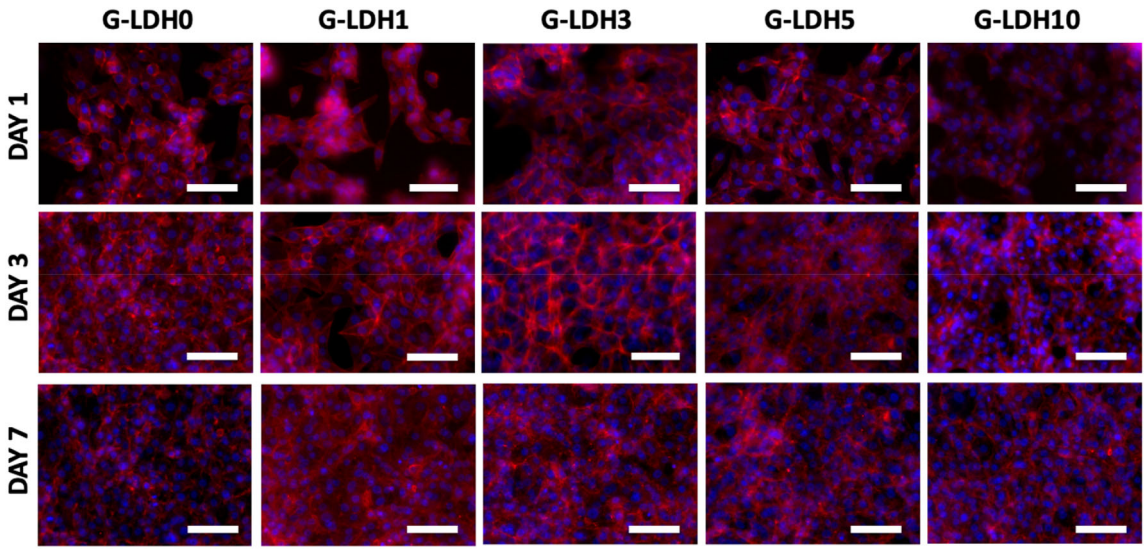

FIGURE 5 In vitro cell adhesion on GelMA/LDHs hydrogel based nanocomposite scaffolds on day 1, 3, and 7. GelMA/LDHs nanocomposite scaffolds supported osteoblast adhesion and spreading as determined by Phalloidin / DAPI staining ($n = 4$) (Scale bar: 100 μm)

Rhodamine-Phalloidin / DAPI staining on day 1, 3, and 7 were demonstrated in Figure 5. It was confirmed that all were exhibited a good cytocompatibility, where osteoblast cells could be easily attached to the surfaces of scaffolds. Therefore, the proposed nanocomposite scaffolds are promising for bone tissue engineering applications.

3.5.2 | 3D bioprinting of cell laden hydrogel based scaffolds

Following defining cell adhesion on optimized hydrogel based nanocomposite bioinks, we investigated the printability of our bioink in the presence of cells. Importantly, extrusion based bioprinting allows researchers to build bioinks with high-viscosity and high cell densities. However, high shear stresses could result in moderate cell viability such as 40%–80%.[5] Herein, we used Live/Dead staining to define the viability of the encapsulated osteoblasts in bioprinted hydrogel constructs to evaluate the influence of the shear stress on the cell viability during extrusion (Figure 6A). As shown in Figure 6B, each of the bioinks (G-LDH0 and G-LDH3) presented high cellular viability (>85%) after bioprinting process. Based on these findings, cells were not affected by the applied shear stress during extrusion that could be attributed to barrier function of hydrogel structure to protect encapsulated cells against shear stresses caused by friction. Furthermore, the viability results on day 3 and 7 demonstrated that cells encapsulated in 3D-structure could easily access nutrients to maintain their viability.

PrestoBlue test was performed to determine the mitochondrial activity and proliferation of bioprinted cells. The PrestoBlue data shown in Figure 6C indicated the proliferation of cells within bioprinted structures G-LDH0 and G-LDH3 increased gradually and significantly over the course of the 1, 3, 5 and 7 days in culture. Notably, the presence of LDHs allowed a sharper increase (around 2.015 fold) in the proliferation rate of osteoblast cells. Taken together, these data proved that LDHs nanoparticles could enhance the proliferation rate of cells and also the proliferation rates of osteoblast cells in bioprinted G-LDH3 composition were higher than that of structures without LDHs. Besides the direct effect of LDHs on the cell proliferation, we realize that the larger pore sizes of G-LDH3 scaffold could led cells to spread and proliferate with an agreement to previous literature.[88,89]

Rhodamine-Phalloidin and DAPI stainings were further used to examine bioprinted cell morphology and spreading within nanocomposite scaffolds (Figure 6D). The fluorescence microscopy images indicated that after 24 h of culture, the osteoblast cells are in spherical morphology, while the cells spread better in the structure over 3 and 7 days in culture. Importantly, we observed that the cellular spreading was promoted in the presence of G-LDH3 compared to G-LDH0. Since the spreading of cells is strongly dependent to the stiffness and pore size of the substrate, we interpreted to these results higher mechanical strength and larger pore size of LDHs incorporated structures as well as directly favorable effect of LDHs on cell spreading.[88,89]

The cellular features including mean cell area and cell aspect ratio was evaluated to quantify the morphological differences. Cells encapsulated in G-LDH3 had a larger cell spreading area than those encapsulated in G-LDH0 (Figure 6E). After 7 days, the mean cell area for cells encapsulated in G-LDH3 (10,851 ± 2283 μm^2) is about 1.211 times higher than encapsulated in G-LDH0 (8961 ± 1879 μm^2) ($p > .05$). Notably, compared to day 1 and day 7, cell-spreading area was 3.096 and 3.814 times larger for G-LDH0 and G-LDH3, respectively. In addition, cell elongation was investigated measuring the short and long axes of the selected cells. Cell elongation was reported as the cellular aspect ratio (long/short axis) where a value of 1 indicates an entirely circular cell.[71] Cells encapsulated in G-LDH3 had a higher cell aspect ratio than those encapsulated in G-LDH0 (Figure 6F). After 7 days, cell aspect ratio for cells encapsulated in G-LDH3 (2.407 ± 1.113) is about 1.272

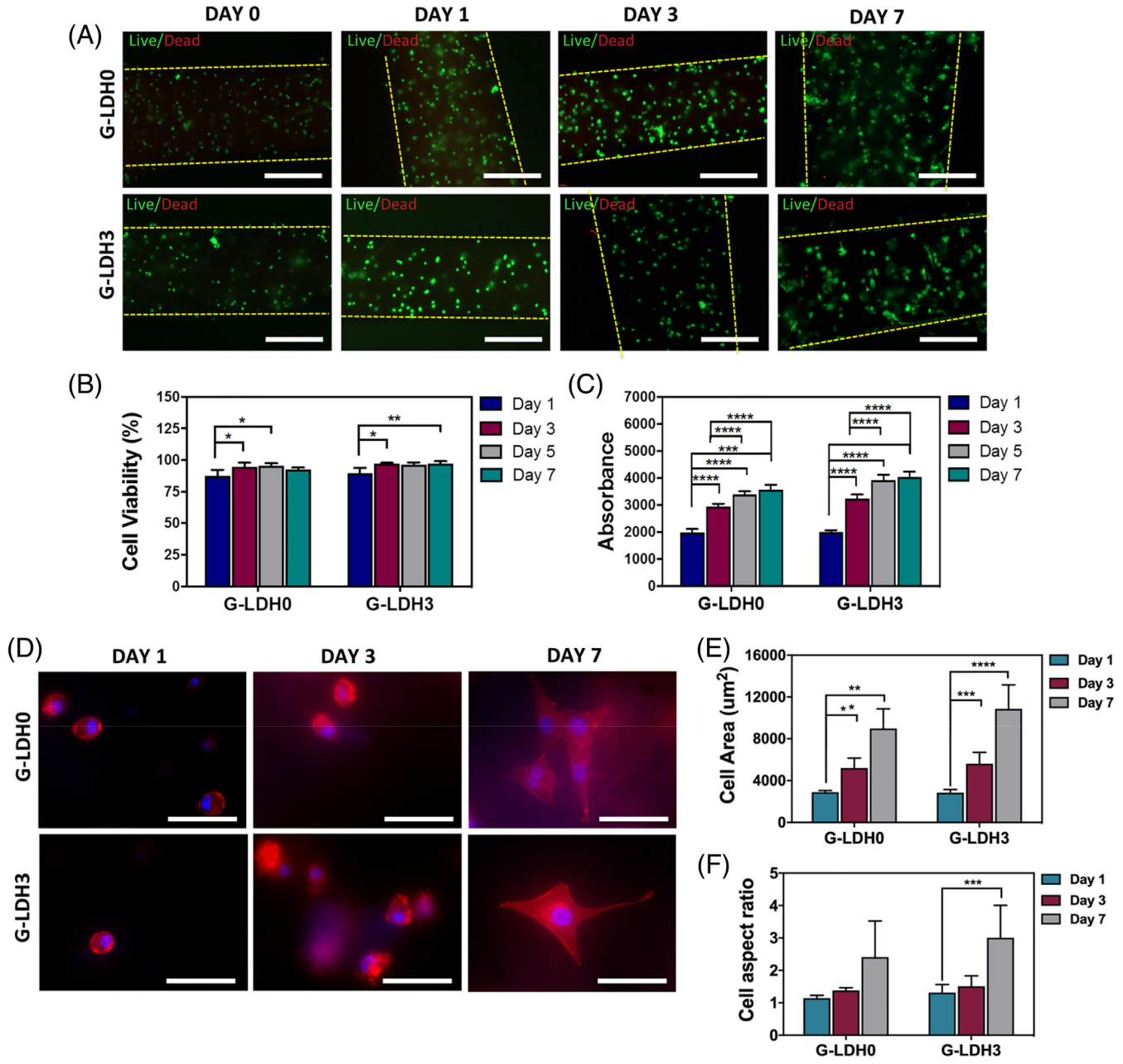

FIGURE 6 In vitro characterization of osteoblast laden 3D bioprinted GelMA/LDHs hydrogel based nanocomposite scaffolds: (A) Live/Dead assay confirmed viability of the encapsulated osteoblasts in bioprinted GelMA/LDHs nanocomposite scaffolds ($n = 3$) (Scale bar: 50 μm), (B) The viability of GelMA/LDHs nanocomposite scaffolds was higher than >85% calculated from Live/Dead assay, (C) The PrestoBlue results confirmed the gradual increase in the proliferation of cells in bioprinted G-LDH0 and G-LDH3 over 1, 3, 5 and 7 days in culture ($n = 6$), (D) Rhodamine-Phalloidin and DAPI staining demonstrated bioprinted cell morphology and spreading within GelMA/LDHs nanocomposite scaffolds nanocomposite scaffolds ($n = 3$) (Scale bar: 400 μm), (E) The cell area of the osteoblast cells encapsulated in G-LDH0 and G-LDH3 on days 1, 3 and 7. Cellular spreading area enhanced by the presence of LDHs, and (F) The cell aspect ratio (long/short axis) of the osteoblast cells encapsulated in G-LDH0 and G-LDH3 on days 1, 3 and 7. Cell aspect ratio increased by the presence of LDHs ($n = 4$). The bar graphs demonstrate the average ± standard deviation (SD) bars. (ns > 0.05,*$p < .05$, **$p < .01$; ***$p < .001$; ****$p < .0001$)

times higher than encapsulated in G-LDH0 (3.061 ± 0.778) ($p > .05$). In particular, compared to day 1 and day 7, cell aspect ratio was 2.108 and 2.331 times higher for G-LDH0 and G-LDH3, respectively. As a result, cells encapsulated in G-LDH3 had a larger cell spreading area and higher cell aspect than those encapsulated in G-LDH0 indicating favorable effect of LDHs on cellular morphology.

4 | CONCLUSION

In this study, we have presented bioactive hydrogel bioinks based on nanocomposite GelMA/LDHs for 3D extrusion bioprinting with high printability, shape fidelity, stiffness, and osteoinductivity. LDHs presented a wide range of interest owing to their multifunctionality in drug delivery,

nanomedicine, and bioengineering. The addition of LDHs into GelMA network could accelerate the physical and biological properties of the nanocomposite scaffolds. Importantly, the osteogenic effect of LDHs in the absence of growth factor makes them a favorable candidate for bone related applications. Firstly, we successfully synthetized LDHs and showed their biocompatibility. Then, we optimized nanocomposite bioink composition to maximize printability, shape fidelity after printing, and mechanical properties. The addition of LDHs was improved the properties of the bioink for extrusion bioprinting and lead to a continuous extrusion to the construction of stable structures with well-defined geometry and shape fidelity. Mechanical features of nanocomposite scaffolds were significantly enhanced by the presence of LDHs. When incorporated into scaffolds, LDHs increased porosity, and enhanced degradation time. Further, bioprinted nanocomposite constructs possessed high cell adhesion and proliferation. Importantly, osteoblasts encapsulated in the nanocomposite bioinks exhibited high cellular viability, spreading, and proliferation. In addition, cells encapsulated in G-LDH3 had a larger cell spreading area and higher cell aspect ratio than those encapsulated in G-LDH0. These data suggest that this growth factor free approach could have a potential for patient specific bone regeneration. Overall, the GelMA-LDHs nanocomposite hydrogel bioinks revealed high structural, mechanical, and biological feasibility for bone related applications and we envision that these nanocomposite scaffolds will present a favorable option to the clinicians for the treatment of bone defects.

AUTHOR CONTRIBUTIONS

Emine Alarçin: Conceptualization, Methodology, Formal analysis, Investigation, Writing – original draft, Writing – review & editing. **Burçin İzbudak:** Methodology, Investigation, Writing – review & editing. **Elif Yüce Erarslan:** Methodology, Investigation, Writing – review & editing. **Sherif Domingo:** Investigation, Writing – review & editing. **Rumeysa Tutar:** Methodology, Formal analysis, Investigation. **Kariman Titi:** Methodology, Formal analysis, Investigation. **Banu Kocaaga:** Methodology, Formal analysis, Investigation, Writing – review & editing. **F. Seniha Guner:** Methodology, Writing – review & editing. **Ayça Bal-Öztürk:** Conceptualization, Supervision, Project administration, Resources, Methodology, Formal analysis, Investigation, Writing – original draft, Writing – review & editing.

ACKNOWLEDGMENTS

This study was funded by the Scientific and Technological Research Council of Turkey (TÜBİTAK) (Grant Number 118S546).

CONFLICT OF INTEREST

The authors declare no conflicts of interest.

DATA AVAILABILITY STATEMENT

The data that support the findings of this study are available from the corresponding author upon reasonable request.

ORCID

Emine Alarçin https://orcid.org/0000-0003-1352-5239
Ayça Bal-Öztürk https://orcid.org/0000-0002-6502-528X

REFERENCES

1. Ashammakhi N, Hasan A, Kaarela O, et al. Advancing Frontiers in bone bioprinting. *Adv Healthc Mater*. 2019;8(7):1801048.
2. Singh S, Choudhury D, Yu F, Mironov V, Naing MW. In situ bioprinting–bioprinting from benchside to bedside? *Acta Biomater*. 2020;101:14-25.
3. Murphy SV, Atala A. 3D bioprinting of tissues and organs. *Nat Biotech*. 2014;32(8):773-785.
4. Anada T, Pan C-C, Stahl AM, et al. Vascularized bone-mimetic hydrogel constructs by 3D bioprinting to promote osteogenesis and angiogenesis. *Int J Mol Sci*. 2019;20(5):1096.
5. Heinrich M, Liu W, Jimenez A, et al. 3D bioprinting: from benches to translational applications. *Small*. 2019;15:1805510.
6. Liu W, Heinrich MA, Zhou Y, et al. Extrusion bioprinting of shear-thinning gelatin Methacryloyl bioinks. *Adv Healthc Mater*. 2017;6(12):1601451.
7. Mazzocchi A, Devarasetty M, Huntwork R, Soker S, Skardal A. Optimization of collagen type I-hyaluronan hybrid bioink for 3D bioprinted liver microenvironments. *Biofabrication*. 2018;11(1):015003.
8. Indurkar A, Bangde P, Gore M, Reddy P, Jain R, Dandekar P. Optimization of guar gum-gelatin bioink for 3D printing of mammalian cells. *Bioprinting*. 2020;20:e00101.
9. Gao T, Gillispie GJ, Copus JS, et al. Optimization of gelatin–alginate composite bioink printability using rheological parameters: a systematic approach. *Biofabrication*. 2018;10(3):034106.
10. Malda J, Visser J, Melchels FP, et al. 25th anniversary article: engineering hydrogels for biofabrication. *Adv Mater*. 2013;25(36):5011-5028.
11. Cofiño C, Perez-Amodio S, Semino CE, Engel E, Mateos-Timoneda MA. Development of a self-assembled peptide/methylcellulose-based bioink for 3D bioprinting. *Macromol Mater Eng*. 2019;304(11):1900353.
12. Singh YP, Bandyopadhyay A, Mandal BB. 3D bioprinting using cross-linker-free silk–gelatin bioink for cartilage tissue engineering. *ACS Appl Mater Interfaces*. 2019;11(37):33684-33696.
13. Annabi N, Tamayol A, Uquillas JA, et al. 25th anniversary article: rational design and applications of hydrogels in regenerative medicine. *Adv Mater*. 2014;26(1):85-124.
14. Heo DN, Castro NJ, Lee S-J, Noh H, Zhu W, Zhang LG. Enhanced bone tissue regeneration using a 3D printed microstructure incorporated with a hybrid nano hydrogel. *Nanoscale*. 2017;9(16):5055-5062.
15. Moncal KK, Ozbolat V, Datta P, Heo DN, Ozbolat IT. Thermally-controlled extrusion-based bioprinting of collagen. *J Mater Sci Mater Med*. 2019;30(5):1-14.
16. Liu W, Zhong Z, Hu N, et al. Coaxial extrusion bioprinting of 3D microfibrous constructs with cell-favorable gelatin methacryloyl microenvironments. *Biofabrication*. 2018;10(2):024102.
17. Kim E, Seok JM, Bae SB, Park SA, Park WH. Silk fibroin enhances cytocompatibilty and dimensional stability of alginate hydrogels for light-based three-dimensional bioprinting. *Biomacromolecules*. 2021;22(5):1921-1931.
18. Zhu K, Chen N, Liu X, et al. A general strategy for extrusion bioprinting of bio-macromolecular bioinks through alginate-templated dual-stage crosslinking. *Macromol Biosci*. 2018;18(9):1800127.
19. Gao Q, He Y, Fu J-z, Liu A, Ma L. Coaxial nozzle-assisted 3D bioprinting with built-in microchannels for nutrients delivery. *Biomaterials*. 2015;61:203-215.
20. Yue K, Trujillo-de Santiago G, Alvarez MM, Tamayol A, Annabi N, Khademhosseini A. Synthesis, properties, and biomedical applications of gelatin methacryloyl (GelMA) hydrogels. *Biomaterials*. 2015;73:254-271.
21. Kazemzadeh-Narbat M, Rouwkema J, Annabi N, et al. Engineering photo cross linkable bicomponent hydrogel constructs for creating 3D vascularized bone. *Adv Healthc Mater*. 2017;6(10):1601122.
22. Born LJ, McLoughlin ST, Dutta D, et al. Sustained released of bioactive mesenchymal stromal cell-derived extracellular vesicles from 3D-

printed gelatin methacrylate hydrogels. *J Biomed Mater Res A*. 2022; 110(6):1190-1198.
23. Radhakrishnan J, Subramanian A, Krishnan UM, Sethuraman S. Injectable and 3D bioprinted polysaccharide hydrogels: from cartilage to osteochondral tissue engineering. *Biomacromolecules*. 2017;18(1):1-26.
24. Billiet T, Gevaert E, De Schryver T, Cornelissen M, Dubruel P. The 3D printing of gelatin methacrylamide cell-laden tissue-engineered constructs with high cell viability. *Biomaterials*. 2014;35(1):49-62.
25. Xing Q, Yates K, Vogt C, Qian Z, Frost MC, Zhao F. Increasing mechanical strength of gelatin hydrogels by divalent metal ion removal. *Sci Rep*. 2014;4(1):1-10.
26. Kim MH, Lee YW, Jung W-K, Oh J, Nam SY. Enhanced rheological behaviors of alginate hydrogels with carrageenan for extrusion-based bioprinting. *J Mech Behav Biomed Mater*. 2019;98:187-194.
27. Bertassoni LE, Cardoso JC, Manoharan V, et al. Direct-write bioprinting of cell-laden methacrylated gelatin hydrogels. *Biofabrication*. 2014;6(2):024105.
28. Chimene D, Miller L, Cross LM, Jaiswal MK, Singh I, Gaharwar AK. Nanoengineered osteoinductive bioink for 3D bioprinting bone tissue. *ACS Appl Mater Interfaces*. 2020;12(14):15976-15988.
29. Rastin H, Ormsby RT, Atkins GJ, Losic D. 3D bioprinting of methylcellulose/gelatin-methacryloyl (MC/GelMA) bioink with high shape integrity. *ACS Appl Bio Mater*. 2020;3(3):1815-1826.
30. Zhou X, Nowicki M, Cui H, et al. 3D bioprinted graphene oxide-incorporated matrix for promoting chondrogenic differentiation of human bone marrow mesenchymal stem cells. *Carbon*. 2017;116: 615-624.
31. Aldana AA, Valente F, Dilley R, Doyle B. Development of 3D bioprinted GelMA-alginate hydrogels with tunable mechanical properties. *Bioprinting*. 2021;21:e00105.
32. Kim J, Hope CM, Gantumur N, et al. Encapsulation of human natural and induced regulatory T-cells in IL-2 and CCL1 supplemented alginate-GelMA hydrogel for 3D bioprinting. *Adv Funct Mater*. 2020; 30(15):2000544.
33. Krishnamoorthy S, Zhang Z, Xu C. Biofabrication of three-dimensional cellular structures based on gelatin methacrylate–alginate interpenetrating network hydrogel. *J Biomater Appl*. 2019;33(8):1105-1117.
34. Datta P, Vyas V, Dhara S, Chowdhury AR, Barui A. Anisotropy properties of tissues: a basis for fabrication of biomimetic anisotropic scaffolds for tissue engineering. *J Bionic Eng*. 2019;16(5):842-868.
35. Yang J, Deng C, Shafiq M, et al. Localized delivery of FTY-720 from 3D printed cell-laden gelatin/silk fibroin composite scaffolds for enhanced vascularized bone regeneration. *Smart Mater Med*. 2022;3: 217-229.
36. Xiang Y, Wang W, Gao Y, et al. Production and characterization of an integrated multi-layer 3D printed PLGA/GelMA scaffold aimed for bile duct restoration and detection. *Front Bioeng Biotechnol*. 2020;8:971.
37. Buyuksungur S, Hasirci V, Hasirci N. 3D printed hybrid bone constructs of PCL and dental pulp stem cells loaded GelMA. *J Biomed Mater Res A*. 2021;109(12):2425-2437.
38. Gaharwar AK, Peppas NA, Khademhosseini A. Nanocomposite hydrogels for biomedical applications. *Biotechnol Bioeng*. 2014;111(3): 441-453.
39. Li W, Wang J, Ren J, Qu X. 3D graphene oxide–polymer hydrogel: near-infrared light-triggered active scaffold for reversible cell capture and on-demand release. *Adv Mater*. 2013;25(46):6737-6743.
40. Paul A, Hasan A, Al Kindi H, et al. Shum-Tim D and others. Injectable graphene oxide/hydrogel-based angiogenic gene delivery system for vasculogenesis and cardiac repair. *ACS Nano*. 2014;8(8):8050-8062.
41. Zeng X, McCarthy DT, Deletic A, Zhang X. Silver/reduced graphene oxide hydrogel as novel bactericidal filter for point-of-use water disinfection. *Adv Funct Mater*. 2015;25(27):4344-4351.
42. Alarçin E, Lee TY, Karuthedom S, et al. Injectable shear-thinning hydrogels for delivering osteogenic and angiogenic cells and growth factors. *Biomater Sci*. 2018;6(6):1604-1615.
43. Huab Z, Chen G. Hydrogels containing layered double hydroxide nanosheets: rheological behavior and excellent stabilities3. *RSC Adv*. 2013;3(12021):12021.
44. Hu Z, Chen G. Aqueous dispersions of layered double hydroxide/polyacrylamide nanocomposites: preparation and rheology. *J Mater Chem A*. 2014;2(33):13593-13601.
45. Xu K, Chen G, Shen J. Exfoliation and dispersion of micrometer-sized LDH particles in poly (ethylene terephthalate) and their nanocomposite thermal stability. *Appl Clay Sci*. 2013;75:114-119.
46. Dutta J, Chatterjee T, Naskar K. LDH as a multifunctional additive in EVA/TPU blends: influence on mechanical, thermal, rheological and flame retardancy properties. *Mater Sci Eng B*. 2018;236:84-94.
47. Izbudak B, Cecen B, Anaya I, Miri AK, Bal-Ozturk A, Karaoz E. Layered double hydroxide-based nanocomposite scaffolds in tissue engineering applications. *RSC Adv*. 2021;11(48):30237-30252.
48. Fayyazbakhsh F, Solati-Hashjin M, Keshtkar A, Shokrgozar MA, Dehghan MM, Larijani B. Novel layered double hydroxides-hydroxyapatite/gelatin bone tissue engineering scaffolds: fabrication, characterization, and in vivo study. *Mater Sci Eng C*. 2017;76: 701-714.
49. Naik VV, Vasudevan S. Sol–gel transition in dispersions of layered double-hydroxide nanosheets. *Langmuir*. 2011;27(21):13276-13283.
50. JB A áS. Rheology and microstructure of aqueous layered double hydroxide dispersions. *J Mater Chem*. 1996;6(5):871-877.
51. Mishra G, Dash B, Pandey S. Layered double hydroxides: a brief review from fundamentals to application as evolving biomaterials. *Appl Clay Sci*. 2018;153:172-186.
52. Chen W, Feng L, Qu B. Preparation of nanocomposites by exfoliation of ZnAl layered double hydroxides in nonpolar LLDPE solution. *Chem Mater*. 2004;16(3):368-370.
53. Chakraborty S, Kumar M, Suresh K, Pugazhenthi G. Influence of organically modified NiAl layered double hydroxide (LDH) loading on the rheological properties of poly (methyl methacrylate)(PMMA)/LDH blend solution. *Powder Technol*. 2014;256:196-203.
54. Zhang J, Ma X, Lin D, et al. Magnesium modification of a calcium phosphate cement alters bone marrow stromal cell behavior via an integrin-mediated mechanism. *Biomaterials*. 2015;53:251-264.
55. Tan J, Wang D, Cao H, Qiao Y, Zhu H, Liu X. Effect of local alkaline microenvironment on the behaviors of bacteria and osteogenic cells. *ACS Appl Mater Interfaces*. 2018;10(49):42018-42029.
56. Kang H, Kim M, Feng Q, et al. Nanolayered hybrid mediates synergistic co-delivery of ligand and ligation activator for inducing stem cell differentiation and tissue healing. *Biomaterials*. 2017;149: 12-28.
57. Huang H, Xu J, Wei K, et al. Bioactive nanocomposite poly (ethylene glycol) hydrogels cross-linked by multifunctional-layered double hydroxides nanocrosslinkers. *Macromol Biosci*. 2016;16(7):1019-1026.
58. Tammaro L, Vittoria V, Calarco A, Petillo O, Riccitiello F, Peluso G. Effect of layered double hydroxide intercalated with fluoride ions on the physical, biological and release properties of a dental composite resin. *J Dent*. 2014;42(1):60-67.
59. Cao D, Xu Z, Chen Y, Ke Q, Zhang C, Guo Y. Ag-loaded MgSrFe-layered double hydroxide/chitosan composite scaffold with enhanced osteogenic and antibacterial property for bone engineering tissue. *J Biomed Mater Res B Appl Biomater*. 2018;106(2):863-873.
60. Jia W, Gungor-Ozkerim PS, Zhang YS, et al. Direct 3D bioprinting of perfusable vascular constructs using a blend bioink. *Biomaterials*. 2016;106:58-68.
61. Özgümüş S, Gök MK, Bal A, Güçlü G. Study on novel exfoliated polyampholyte nanocomposite hydrogels based on acrylic monomers and Mg–Al–Cl layered double hydroxide: synthesis and characterization. *Chem Eng J*. 2013;223:277-286.
62. Xu ZP, Stevenson GS, Lu C-Q, Lu GQ, Bartlett PF, Gray PP. Stable suspension of layered double hydroxide nanoparticles in aqueous solution. *J Am Chem Soc*. 2006;128(1):36-37.

63. Yan S, Gu W, Zhang B, Rolfe BE, Xu ZP. High adjuvant activity of layered double hydroxide nanoparticles and nanosheets in anti-tumour vaccine formulations. *Dalton Trans*. 2018;47(9):2956-2964.
64. Nichol JW, Koshy ST, Bae H, Hwang CM, Yamanlar S, Khademhosseini A. Cell-laden microengineered gelatin methacrylate hydrogels. *Biomaterials*. 2010;31(21):5536-5544.
65. Choi BY, Chalisserry EP, Kim MH, Kang HW, Choi I-W, Nam SY. The influence of astaxanthin on the proliferation of adipose-derived mesenchymal stem cells in gelatin-methacryloyl (GelMA) hydrogels. *Materials*. 2019;12(15):2416.
66. Ouyang L, Yao R, Zhao Y, Sun W. Effect of bioink properties on printability and cell viability for 3D bioplotting of embryonic stem cells. *Biofabrication*. 2016;8(3):035020.
67. Kyle S, Jessop ZM, Al-Sabah A, Whitaker IS. 'Printability'of candidate biomaterials for extrusion based 3D printing: state-of-the-art. *Adv Healthc Mater*. 2017;6(16):1700264.
68. Saygili E, Kaya E, Ilhan-Ayisigi E, et al. An alginate-poly (acrylamide) hydrogel with TGF-β3 loaded nanoparticles for cartilage repair: biodegradability, biocompatibility, and protein adsorption. *Int J Biol Macromol*. 2021;172:381-393.
69. Zhang H, Yang S, Masako N, Lee DJ, Cooper LF, Ko C-C. Proliferation of preosteoblasts on TiO2 nanotubes is FAK/RhoA related. *RSC Adv*. 2015;5(48):38117-38124.
70. Jhala D, Rather H, Vasita R. Polycaprolactone–chitosan nanofibers influence cell morphology to induce early osteogenic differentiation. *Biomater Sci*. 2016;4(11):1584-1595.
71. Chen P, Miyake M, Tsukamoto M, Tsutsumi Y, Hanawa T. Response of preosteoblasts to titanium with periodic micro/nanometer scale grooves produced by femtosecond laser irradiation. *J Biomed Mater Res A*. 2017;105(12):3456-3464.
72. Shamsayei M, Yamini Y, Asiabi H, Safari M. On-line packed magnetic in-tube solid phase microextraction of acidic drugs such as naproxen and indomethacin by using Fe. *Mikrochim Acta*. 2018;185(3):192.
73. Yan L, Chen W, Zhu X, et al. Folic acid conjugated self-assembled layered double hydroxide nanoparticles for high-efficacy-targeted drug delivery. *Chem Commun (Camb)*. 2013;49(93):10938-10940.
74. Olfs HW, Torres-Dorante LO, Eckelt R, Kosslick H. Comparison of different synthesis routes for Mg–Al layered double hydroxides (LDH): characterization of the structural phases and anion exchange properties. *Appl Clay Sci*. 2009;43(3–4):459-464.
75. Nogueira KAB, Cecilia JA, Santos SO, et al. Adsorption behavior of bovine serum albumin on Zn–Al and Mg–Al layered double hydroxides. *J Sol-Gel Sci Technol*. 2016;80(3):748-758.
76. Becker CM, Gabbardo AD, Wypych F, Amico SC. Mechanical and flame-retardant properties of epoxy/Mg–Al LDH composites. *Compos A: Appl Sci Manuf*. 2011;42(2):196-202.
77. Xing K, Wang H, Guo L, Song W, Zhao Z. Adsorption of tripolyphosphate from aqueous solution by Mg–Al–CO3-layered double hydroxides. *Colloids Surf A Physicochem Eng Asp*. 2008;328(1–3):15-20.
78. Theiss FL, Ayoko GA, Frost RL. Iodide removal using LDH technology. *Chem Eng J*. 2016;296:300-309.
79. Azouri A, Ge M, Xun K, Sattler K, Lichwa J, Ray C. Zeta potential studies of titanium dioxide and silver nanoparticle composites in water-based colloidal suspension. 2006. 221–223.
80. Wu Y, Zhu R, Zhou Y, et al. Layered double hydroxide nanoparticles promote self-renewal of mouse embryonic stem cells through the PI3K signaling pathway. *Nanoscale*. 2015;7(25):11102-11114.
81. Kang HR, da Costa Fernandes CJ, da Silva RA, Constantino VRL, Koh IHJ, Zambuzzi WF. Mg–Al and Zn–Al layered double hydroxides promote dynamic expression of marker genes in osteogenic differentiation by modulating mitogen-activated protein kinases. *Adv Healthc Mater*. 2018;7(4):1700693.
82. Mamaghani KR, Naghib SM, Zahedi A, Mozafari M. Synthesis and microstructural characterization of GelMa/PEGDA hybrid hydrogel containing graphene oxide for biomedical purposes. *Mater Today Proc*. 2018;5(7):15635-15644.
83. Usal TD, Yucel D, Hasirci V. A novel GelMA-pHEMA hydrogel nerve guide for the treatment of peripheral nerve damages. *Int J Biol Macromol*. 2019;121:699-706.
84. Gillispie GJ, Han A, Uzun-Per M, et al. The influence of printing parameters and cell density on bioink printing outcomes. *Tissue Eng Part A*. 2020;26(23–24):1349-1358.
85. Deo KA, Singh KA, Peak CW, Alge DL, Gaharwar AK. Bioprinting 101: design, fabrication, and evaluation of cell-laden 3D bioprinted scaffolds. *Tissue Eng Part A*. 2020;26(5–6):318-338.
86. Aguado BA, Mulyasasmita W, Su J, Lampe KJ, Heilshorn SC. Improving viability of stem cells during syringe needle flow through the design of hydrogel cell carriers. *Tissue Eng Part A*. 2012;18(7–8):806-815.
87. Almeida JF, Ferreira P, Lopes A, Gil MH. Photo cross linkable biodegradable responsive hydrogels as drug delivery systems. *Int J Biol Macromol*. 2011;49(5):948-954.
88. Wang Z, Abdulla R, Parker B, Samanipour R, Ghosh S, Kim K. A simple and high-resolution stereolithography-based 3D bioprinting system using visible light cross-linkable bioinks. *Biofabrication*. 2015;7(4):045009.
89. O'Brien FJ, Harley BA, Waller MA, Yannas IV, Gibson LJ, Prendergast PJ. The effect of pore size on permeability and cell attachment in collagen scaffolds for tissue engineering. *Technol Health Care*. 2007;15(1):3-17.

SUPPORTING INFORMATION

Additional supporting information can be found online in the Supporting Information section at the end of this article.

How to cite this article: Alarçin E, İzbudak B, Yüce Erarslan E, et al. Optimization of methacrylated gelatin /layered double hydroxides nanocomposite cell-laden hydrogel bioinks with high printability for 3D extrusion bioprinting. *J Biomed Mater Res*. 2022;1-15. doi:10.1002/jbm.a.37450